Nanoscale Horizons

ROYAL SOCIETY OF CHEMISTRY

COMMUNICATION

View Article Online
View Journal | View Issue

Cite this: *Nanoscale Horiz.*, 2025, **10**, 2896

Received 15th June 2025,
Accepted 7th August 2025

DOI: 10.1039/d5nh00418g

rsc.li/nanoscale-horizons

Multifunctional electronic skin integrating dual-mode optical and pressure sensors for caregiving robots

Hyeonjun Heo, †[ab] Jinhong Park,†[c] Daewon Ko,†[de] Kyunghoon Lee,[f] Jinhee Lee,[f] Hyunwoo Joo,[a] Jiwoong Yang,[f] Gi Doo Cha,[g] Dae-Hyeong Kim *[ab] and Dong Chan Kim *[de]

Advancements in artificial intelligence have broadened the capabilities of robots, particularly in caregiving applications that are essential for aging societies facing a growing shortage of human caregivers. Humanoid caregiving robots require sophisticated sensing systems to perform delicate tasks such as monitoring vital signs and providing physical assistance without causing discomfort. In particular, functionalities such as close-range proximity sensing, tactile feedback, and physiological and electrophysiological signal monitoring are essential for ensuring safe and effective caregiving. However, electronic skin (e-skin) capable of simultaneously detecting proximity, tactile, and physiological signals remains largely unexplored. Here, we present a multifunctional robotic e-skin that vertically integrates an optical sensor array and a pressure sensor array. The optical sensor, comprising quantum dot light-emitting diodes (QLEDs) and perovskite photodetectors (PDs), enables dual-mode sensing for both proximity detection and photoplethysmography (PPG) measurement. A carbon nanotube (CNT)-based pressure sensor array provides tactile feedback, ensuring stable and precise physiological monitoring. Additionally, the array structure allows cross-validation of proximity and PPG data, improving measurement accuracy and reliability. This multifunctional e-skin represents a significant advance toward the development of caregiving robots capable of safe, precise, and sophisticated human–robot interaction.

New concepts

With recent advancements in robotics and artificial intelligence (AI), robotic electronic skin (e-skin) incorporating soft electronic sensors and circuits has gained growing attention. These systems aim to enhance human–robot interaction by enabling multifunctional sensing capabilities. In this work, we present a compact robotic e-skin composed of vertically stacked optical and tactile sensor modules and explore its potential for caregiving applications. A key contribution of this study is the demonstration of dual-mode operation within the optical sensing module, which consists of flexible quantum dot light-emitting diode (QLED) arrays and perovskite photodetector (PePD) arrays. First, the optical module functions as a proximity sensor to detect nearby objects or human skin. Combined with the tactile sensor array, this supports precise spatial awareness of targeted objects. Second, upon skin contact, red- and green-emitting QLEDs paired with PePDs enable photoplethysmography (PPG) and pulse oximetry for real-time, non-invasive physiological monitoring. The pressure sensor array further ensures stable contact conditions essential for on-skin sensing. This work presents a practical integration strategy for hybrid optoelectronic–mechanosensory systems in robotics, addressing limitations of conventional bulky components. The proposed robotic e-skin offers a promising foundation for intelligent human–robot interaction in next-generation caregiving technologies.

1. Introduction

As artificial intelligence (AI) and electronic systems continue to advance rapidly, robots are becoming increasingly capable of perceiving their environments and autonomously performing task-specific operations.[1] These advancements have significantly broadened the scope of robotic applications in healthcare, elderly care, and personalized assistance.[2–4] In particular, caregiving robots have emerged as a promising solution to alleviate the burden on healthcare systems in aging societies facing a growing shortage of human caregivers.[5] Humanoid

[a] *Center for Nanoparticle Research, Institute for Basic Science (IBS), Seoul 08826, Republic of Korea. E-mail: dkim98@snu.ac.kr*
[b] *School of Chemical and Biological Engineering, Institute of Chemical Processes, Seoul National University, Seoul 08826, Republic of Korea*
[c] *The Artie McFerrin Department of Chemical Engineering, Texas A&M University, College Station, TX 77843, USA*
[d] *Department of Semiconductor Engineering, Gachon University, Seongnam 13120, Republic of Korea. E-mail: dckim@gachon.ac.kr*
[e] *Department of Chemical and Biological Engineering, Gachon University, Seongnam 13120, Republic of Korea*
[f] *Department of Energy Science and Engineering, Daegu Gyeongbuk Institute of Science and Technology (DGIST), Daegu 42988, Republic of Korea*
[g] *Department of Systems Biotechnology, Chung-Ang University, Ansung, 17546, Republic of Korea*
† These authors contributed equally to this work.

caregiving robots offer distinct advantages due to their human-like interaction capabilities, adaptability, and potential for personalized support.[6] They are well-suited for tasks such as monitoring vital signs, administering medications, and providing physical assistance, thereby enhancing the efficiency and consistency of caregiving services.[7]

To safely and effectively perform such interactive tasks, caregiving robots require advanced sensing platforms that mimic the multifunctional human sensory system.[8–10] These platforms must support precise spatial awareness, gentle physical contact, and reliable physiological signal acquisition.[11,12] Although camera-based vision systems provide rich visual information for object recognition and environmental mapping, they face inherent limitations—particularly in close-range proximity sensing—and cannot directly capture tactile and/or physiological signals. Consequently, there is a growing demand for specialized, multifunctional sensing systems based on electronic skin (e-skin), which can complement vision systems by enabling proximity detection, tactile sensing, and physiological monitoring.[13–17] However, most current solutions rely on separate, bulky, and complex components, restricting their integration into compact robotic structures such as fingertips.[18] Therefore, the development of compact, integrated, and multifunctional e-skins is critical for safe and reliable human–robot interaction.

Optoelectronic devices have gained attention in wearable and biomedical applications due to their high sensitivity, functional versatility, and environmental stability.[19,20] In particular, optical sensors that combine light-emitting diodes (LEDs) and photodetectors (PDs) enable dual-mode sensing capabilities for proximity detection and photoplethysmography (PPG), allowing robots to approach users safely and monitor human health parameters.[21–27] Furthermore, integrating optical sensors with tactile feedback sensors enables safe, gentle, and accurate robotic contact during health signal acquisition.[28] A promising strategy to realize compact and multifunctional robotic e-skin is the vertical integration of dual-mode optical sensing and tactile sensing components. This architecture reduces the system footprint, improves spatial alignment for higher signal fidelity, and facilitates conformal integration onto curved surfaces such as robot fingertips.

In this work, we present a novel multifunctional e-skin designed for humanoid caregiving robots. The system features vertically integrated sensor modules, which incorporate a carbon nanotube (CNT)-based pressure sensor array and an optical sensor array in a stacked configuration. The optical sensor layer combines quantum dot light-emitting diodes (QLEDs)[29–35] and perovskite photodetectors (PePDs),[36–38] enabling dual-mode operation for both proximity sensing and PPG measurements. The pressure sensor array provides tactile feedback, facilitating stable contact and precise acquisition of physiological signals. Furthermore, the pixelated sensor architecture enables cross-validation between proximity and PPG data, enhancing the accuracy and reliability of measurements. This integrated e-skin platform represents a significant advancement toward next-generation caregiving robots, offering safe, accurate, and personalized human–robot interactions in real-world healthcare environments.

2. Results and discussion

2.1. Multifunctional robotic e-skin based on vertically integrated sensing modules

The robotic e-skin is composed of two vertically stacked functional layers: tactile sensor arrays (layer 1) and optical sensor arrays (layer 2) (Fig. 1(a)). Layer 1 featured a 5 × 6 passive-matrix (PM) array of microstructured, resistive pressure sensors for tactile sensing. Layer 2 consisted of a 5 × 6 PM array of PePDs with a 4 × 5 PM array of QLEDs, with 10 pixels emitting red light and the other 10 pixels emitting green light. The PePD and QLED pixels were strategically arranged at alternating grid intersections to avoid overlapping, allowing the PDs to capture light signals reflected from target surfaces. To prevent delamination and maintain structural integrity, adhesive interlayers based on diluted polydimethylsiloxane (PDMS) were placed between adjacent sensor layers. All components were soft and flexible, enabling conformal integration with the curved surfaces of robotic fingertips (Fig. 1(b)).

The e-skin was engineered to support a multi-phased caregiving scenario, comprising (i) approach, (ii) contact and pressure regulation, and (iii) biosignal acquisition (Fig. 1(c)). In the first phase, the optical sensors in layer 2 detected the proximity of human skin as the robotic fingertip approaches. In the second phase, upon contact, the pressure sensors in layer 1 detected tactile input, measuring the contact force between the human and robot to ensure a safe and stable physical interaction. In the third phase, the optical sensors switched to PPG sensing modes and began capturing physiological signals. Each layer was activated sequentially in accordance with the interaction phase, enabling coordinated, multimodal data acquisition (Fig. 1(d)).

This configuration allowed the e-skin to perform comprehensive physiological monitoring, including proximity sensing, tactile feedback, and biosignal collection. A core feature of the system was the dual-mode operation of the optical sensor module, which enabled seamless switching between proximity detection and PPG acquisition. From the collected biosignals, key health metrics such as oxygen saturation can be reliably extracted. Moreover, the use of multiple sensor pixels facilitated simultaneous data collection and cross-validation, enhancing the overall accuracy, reliability, and robustness of the measurements.

2.2. Fabrication of vertically integrated multifunctional robotic e-skin

The robotic e-skin was fabricated through the vertical integration of multi-functional sensor arrays, as illustrated in Fig. 2. Compared to horizontal integration, vertical integration enables efficient use of space, allowing diverse components—such as QLEDs, PePDs, and CNT-based pressure sensors—to be integrated within the limited area of a robotic fingertip

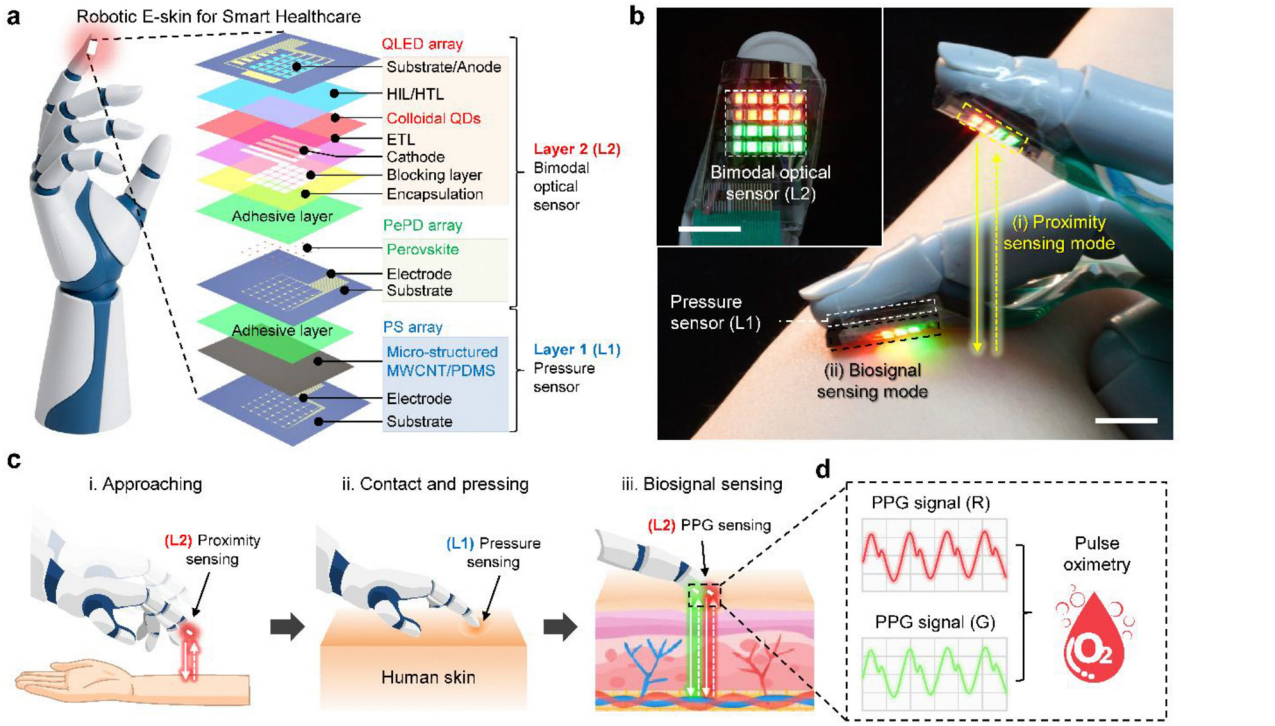

Fig. 1 Vertically integrated multifunctional robotic e-skin. (a) Exploded view of the robotic e-skin comprising vertically stacked dual-mode optical and pressure sensor arrays. (b) Photographs of the e-skin integrated onto robotic fingertips for sensing (i) proximity and (ii) biosignals with tactile feedback. Scale bar, 20 mm. The inset shows the optical sensor array with red and green QLED. Scale bar, 20 mm. (c) Schematic illustration of three representative phases involved in caregiving tasks: (i) proximity sensing during approaching using the optical sensor array, (ii) pressure sensing for contact with an appropriate pressure level, and (iii) PPG sensing using the optical sensor array during biosignal acquisition. (d) Schematic overview of physiological signals captured and derived from the multifunctional robotic e-skin.

(<3 cm $\times$ 3 cm). Monolithic fabrication of all components on a single plane not only reduces the pixel density but also presents significant process challenges due to material and fabrication incompatibilities. To overcome this, each device was fabricated separately on optimized substrates and then vertically stacked, enabling compact, high-density heterogeneous integration. The detailed fabrication process is as follows.

First, a cross-bar passive-matrix (PM) array of flexible QLEDs was fabricated using a layered structure consisting of parylene/epoxy/ITO anodes/PEDOT:PSS (hole injection layer, HIL)/TFB (hole transport layer, HTL)/red and green quantum dots (QDs, emitting layer, EML)/ZnMgO (electron transport layer, ETL)/Al cathodes/parylene/epoxy, as illustrated in Fig. 2(a).[29] Characterization of synthesized CdSe@ZnS QDs is shown in Fig. S1 and S2. The bottom electrodes for the QLEDs were deposited and patterned on a substrate comprising 1 μm of parylene and 0.3 μm of epoxy (Fig. 2(a)-i). For the EMLs, red and green QDs were deposited onto the TFB layer *via* a transfer printing method to enable dual-wavelength emission required for pulse oximetry (Fig. 2(a)-ii).[39] Then, the active layers were encapsulated with top protective layers using the same parylene and epoxy stack as the bottom substrate. After delaminating the flexible QLED array, reactive ion etching (RIE) was used to selectively remove the bottom encapsulation layer and expose the bottom electrodes (Fig. 2(a)-iii). The fabricated flexible QLED array is shown in Fig. 2(a)-iv.

Next, a PM array of flexible PePDs was fabricated on a separate substrate. Each device consists of interdigitated Cr/Au electrodes patterned on a polyimide (PI) substrate, with an insulating epoxy layer applied between them to prevent electrical short-circuits (Fig. 2(b)-i). Perovskite films were then patterned onto the electrode regions using a swelling-induced lift-off process (Fig. 2(b)-ii and iii). The composition of the perovskite film and details of the patterning process follow the previously reported protocol.[40] An optical image of the fabricated PePD array is shown in Fig. 2(b)-iv.

Subsequently, the CNT-based, resistive pressure sensor array was fabricated on a separate substrate, as illustrated in Fig. 2(c). A silicon mold was first patterned by grayscale photolithography of a photoresist layer and treated with a self-assembled monolayer to facilitate mold release (Fig. 2(c)-i). A composite solution of CNTs and polydimethylsiloxane (PDMS) in a 9 : 1 weight ratio was then blade-coated onto the mold and cured to form a microstructured elastomeric sensing layer (Fig. 2(c)-ii). This active layer was subsequently transferred onto a PI substrate with interdigitated Cr/Au electrodes, completing the fabrication of the pressure sensor array (Fig. 2(c)-iii and iv).

Finally, the fabricated devices were vertically integrated to fabricate the multifunctional robotic e-skin (Fig. 2(d)-i). The PePD array was first delaminated and transferred onto a polyethylene terephthalate (PET) substrate coated with

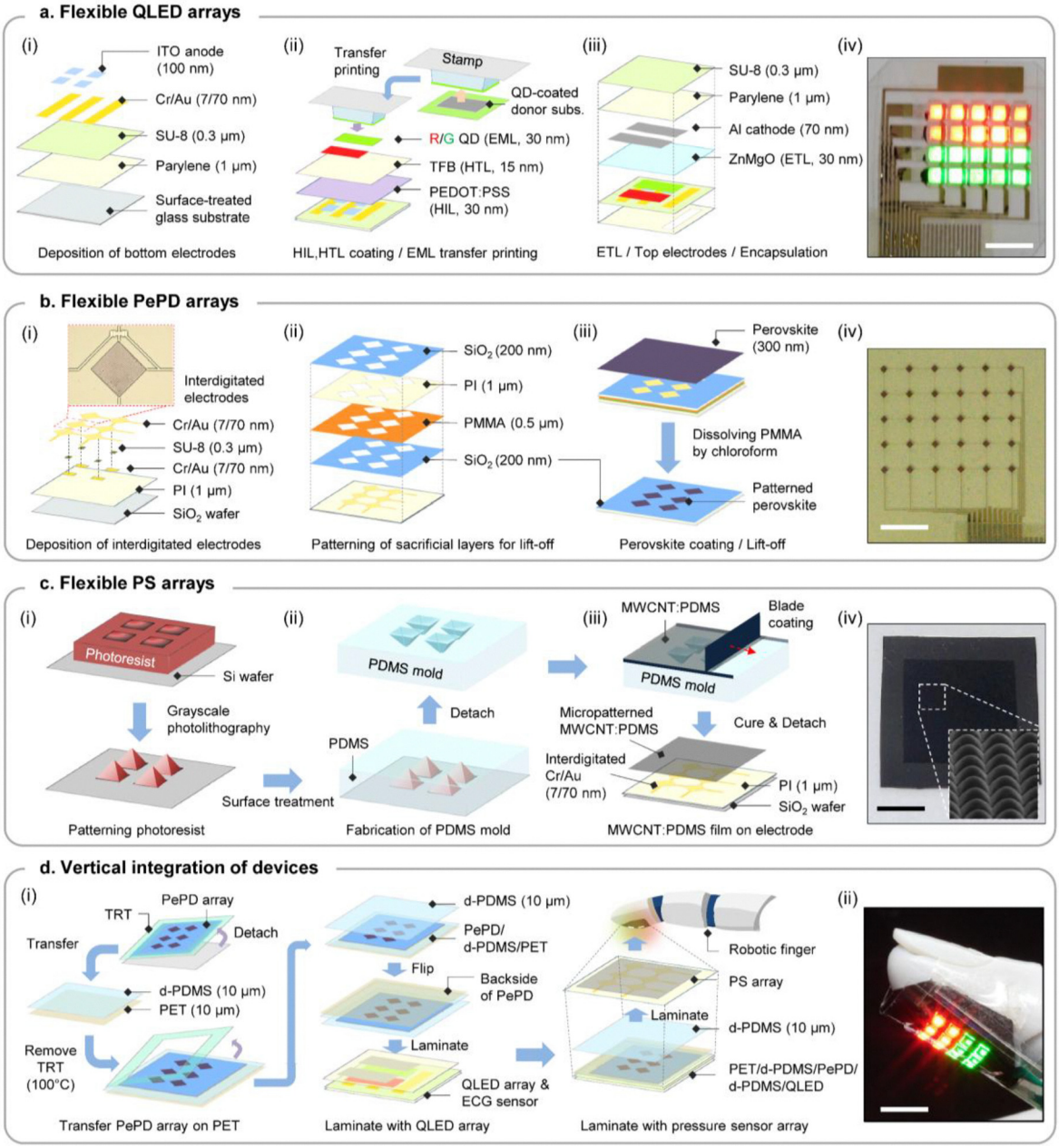

Fig. 2 Fabrication process of vertically integrated multifunctional robotic e-skin. (a) (i)–(iii) Schematic illustrations of the fabrication process for flexible QLED arrays, and (iv) photograph of the QLED array showing red and green emission. Scale bar, 10 mm. (b)-(i)–(iii) Schematic illustrations of the fabrication process for flexible PePD arrays, and (iv) photograph of the completed PePD array. Scale bar, 10 mm. (c)-(i)–(iii) Schematic illustrations of the fabrication process for flexible pressure sensor arrays, and (iv) photograph of the assembled pressure sensor array. The inset shows the microscopic image of the microstructured CNT/PDMS nanocomposite. Scale bar, 10 mm. (d) (i) Schematic illustrations of the vertical integration process for assembling the multifunctional e-skin, and (ii) photograph of the final device integrated onto a robotic fingertip. Scale bar, 10 mm.

diluted PDMS (d-PDMS) using a thermal release tape (TRT). The d-PDMS layer served as an adhesive to prevent delamination. After flipping, the PePD array was laminated onto the flexible QLED array with precise alignment to avoid overlap between the LED and PD pixels, thereby forming a dual-mode optical sensing module. This optical module was then laminated onto the CNT-based pressure sensor array, resulting in a fully integrated, flexible, and multifunctional robotic e-skin. The final system was successfully transferred onto a robotic fingertip (Fig. 2(d)-ii). Detailed procedures for material preparation and device fabrication are described in the Methods section.

2.3. Characterization of optical and pressure sensors

The electrical and optical characteristics of a single pixel in the fabricated optical sensor array were evaluated. As shown in Fig. 3(a), a blocking layer was inserted between the QLED and PePD to prevent direct light absorption by the PePD, thereby

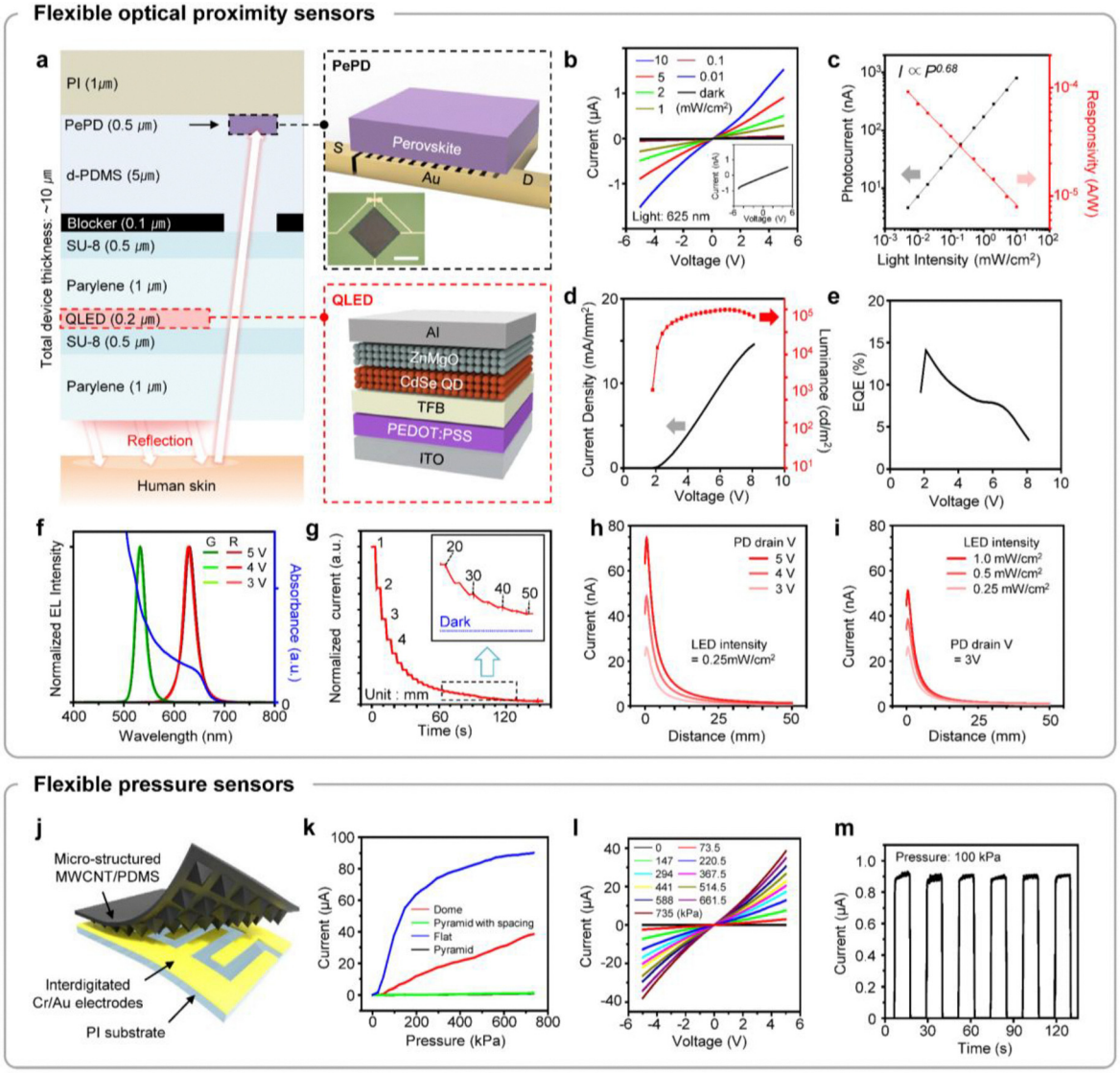

Fig. 3 Characterization of optical proximity and pressure sensors. (a) Schematic illustration of the cross-sectional structure of the optical sensor (left), and detailed structures of the PePD (top right) and QLED (bottom right). The inset image in the top right panel shows a magnified image of the PePD. Scale bar, 500 μm. (b) Current–voltage (*I*–*V*) curves of PePDs under dark conditions and varying illumination intensities at 625 nm. The inset shows the dark current. (c) Photocurrent and responsivity of PePDs as a function of illumination intensity at 625 nm. (d) Current density–voltage–luminance (*J*–*V*–*L*) curves of red QLEDs. (e) External quantum efficiency (EQE) of red QLEDs as a function of voltage. (f) Absorbance spectrum of the perovskite film and normalized EL spectra of red and green QDs under different voltages. (g) Time-resolved current response of the optical sensor under red QLED illumination at different distances between the sensor and a target object. The inset shows the dark current and current responses within the distance range of 20–50 mm. (h) Current as a function of distance under constant red QLED illumination and varying bias voltages applied to the PePD. (i) Current as a function of distance under varying red QLED light intensities at constant PePD bias. (j) Schematic illustration of pressure sensor structure. (k) Pressure-dependent current responses of sensors with varying microstructure geometries under a constant 3 V bias. (l) *I*–*V* curves of pressure sensors under different pressure levels. (m) Transient current response of the pressure sensor under repeated loading/unloading cycles at 100 kPa and a constant 3 V bias.

minimizing optical crosstalk. The photoconductive PePD exhibited symmetric current–voltage (*I*–*V*) response under various illumination intensities from the red QLED (Fig. 3(b)). The photocurrent and responsivity displayed a quasi-linear dependence on the light intensity, following the power-law relationship (Fig. 3(c)). Transient response measurement demonstrated stable photoswitching behavior with consistent performance over repeated cycles (Fig. S3).

The red QLED exhibited outstanding optical output, sufficient to achieve both proximity and PPG sensing capabilities. The maximum brightness of the red QLED was 97 012 nits at 6.6 V (Fig. 3(d)) and the maximum external quantum efficiency (EQE) was 14.1% at 2.1 V (Fig. 3(e)). The bandgap of the perovskite material was engineered to absorb both red and green wavelengths, enabling dual wavelength detection (Fig. 3(f)). Based on these properties, the proximity sensing

capability of the optical sensors was characterized, demonstrating a measurable distance range from approximately 1 mm to 50 mm (Fig. 3(g)-(i)). Additional characterization results using green QLEDs are provided in Fig. S4.

To evaluate the pressure sensing component, individual flexible pressure sensors were fabricated with four different microstructure geometries: pyramid, dome, pyramid with spacing, and flat (Fig. 3(j) and Fig. S5). Among them, the pressure sensor with dome-shaped microstructures exhibited a broad linear response over a wide pressure range, making it the most suitable design for pressure sensing (Fig. 3(k)). The *I–V* characteristics under various pressures showed linear behavior, indicating an Ohmic contact between the CNT/PDMS composite and the interdigitated electrodes (Fig. 3(l)). As applied pressure increased, the electrical resistance decreased due to an enlarged contact area between the microstructured composite and the electrode surface. The pressure sensor also exhibited a stable response under repeated loading/unloading cycles (Fig. 3(m)).

2.4. Demonstration of proximity and tactile sensing for caregiving–relevant interactions

To evaluate the functional capabilities of the integrated multifunctional e-skin, we demonstrated two representative caregiving-relevant scenarios using a robotic fingertip equipped with the fabricated e-skin (Fig. 4). The pixelated architecture of the optical and pressure sensor arrays enabled spatially resolved signal acquisition, allowing for precise localization and stable interaction with small objects and human skin.

In the first scenario, the e-skin was employed to detect and localize a small vitamin tablet. As the fingertip approached the target (Fig. 4(a)-i and ii), current signals were generated in the flexible PePD arrays (Fig. S6). Following pixel-wise calibration, the optical sensor array provided proximity information across the sensing area (Fig. 4(b)-i and ii). Initially, only a subset of pixels exhibited high outputs due to misalignment with the target, indicating the need for further positional adjustment. As the fingertip moved closer and achieved better alignment with the object (Fig. 4(a)-iii), the activated pixels shifted to those directly above the target, confirming accurate positioning (Fig. 4(b)-iii). Once optical alignment was established, the fingertip advanced to make physical contact with the object (Fig. 4(a)-iv). Contact was confirmed by a corresponding increase in the output signals from the pressure sensor array, indicating successful tactile engagement and readiness for subsequent manipulation tasks such as grasping (Fig. 4(b)-iv).

In the second scenario, the fingertip approached and contacted human skin to simulate the conditions required for biosignal acquisition. Similar to the first scenario, current signals generated in flexible PePD arrays and PS arrays are calibrated to the proximity and tactile information, respectively (Fig. S7). As the fingertip neared the skin surface (Fig. 4(c)-i), the optical sensor array operated in the proximity sensing mode, providing real-time distance information between the fingertip and the skin (Fig. 4(d)-i). Due to the curved shape of the fingertip, the central rows of pixels, which were positioned closer to the skin, exhibited higher photocurrent signals than those at the edges. Since contact had not yet occurred at this stage, the pressure sensor array did not exhibit any significant output (Fig. 4(e)-i).

Upon initial contact with the skin (Fig. 4(c)-ii), all pixels in the optical sensor array reached saturation (Fig. 4(d)-ii), while the pressure sensor array began generating tactile signals (Fig. 4(e)-ii). At this point, the dual-modal optical sensor array transitioned from proximity sensing to the PPG sensing mode. Controlled pressure was subsequently applied to maintain stable contact and enable accurate PPG signal acquisition (Fig. 4(c)–(e)-iii). The physiological measurements obtained in this process will be discussed in the following section. After biosignal acquisition was completed, the fingertip was withdrawn (Fig. 4(c)-iv), prompting the optical sensor array to revert to the proximity sensing mode (Fig. 4(d)-iv), while the pressure sensor array again displayed no significant output (Fig. 4(e)-iv).

2.5. Demonstration of physiological and electrophysiological signal sensing

The biosignal sensing capabilities of the integrated multifunctional e-skin were demonstrated by acquiring on-skin PPG signals. As shown in Fig. 5(a), four PePD pixels (P1, P2, P3, P4), located between the upper 10 pixels of red QLEDs and the lower 10 pixels of green QLEDs, were selected among the total 30 PePD pixels of the optical sensor array, to measure PPG signals under red and green illumination. As discussed in the previous section, the optical sensor array provided dual-mode functionality—proximity and PPG sensing—depending on the presence of contact. These modes were distinguished based on tactile signals that served as an indicator of physical contact and appropriate pressure levels (Fig. 5(b)). Under a contact pressure of $\sim$20 kPa, which ensures a stable contact between the device and the skin, the e-skin successfully captured PPG waveforms using both red and green QLED illumination (Fig. 5(c)).

In addition to contact pressure, the position of the sensor on the body can significantly influence PPG signal quality. Factors such as variations in vascular distribution, skin thickness, and tissue compression can all contribute to signal variability.[41] Consequently, single-pixel PPG sensors may exhibit reduced accuracy due to their inability to capture these spatial variations. In this context, the pixelated architecture of the e-skin offers a distinct advantage by enabling spatially resolved signal acquisition that compensates for such effects.

As illustrated in Fig. 5(d) and (e), each of the four pixels recorded PPG signals under both red and green illumination, with variations in amplitude and clarity depending on the pixel position. These spatial differences can impact the accuracy of physiological parameters derived from PPG signals, such as heart rate and peripheral oxygen saturation (SpO_2). While conventional pulse oximeters typically use red and infrared light, previous studies have shown that red and green light combinations can also support reliable SpO_2 estimation.[42]

To evaluate the impact of pixel position on measurement accuracy, SpO_2 levels were estimated from the PPG

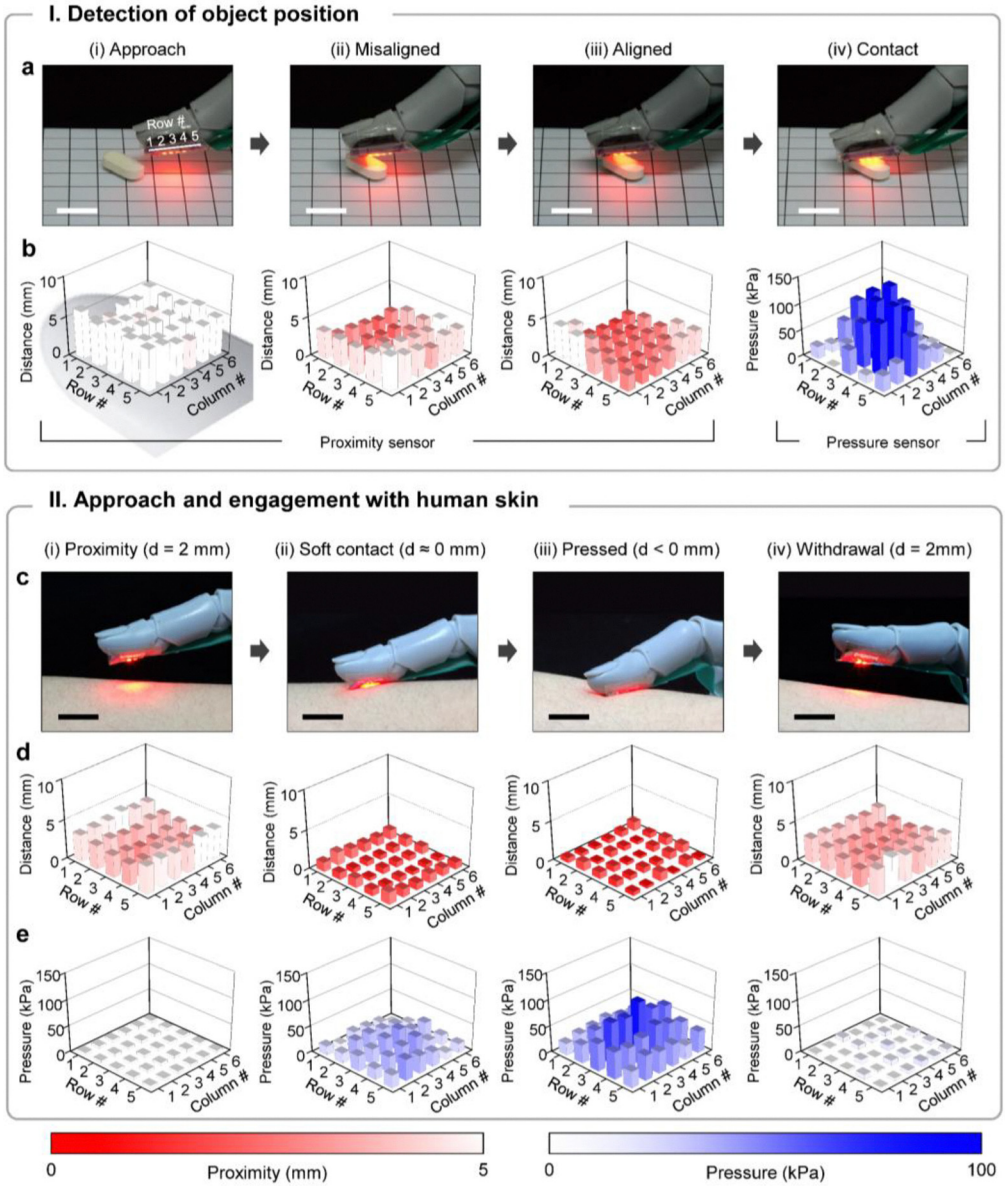

Fig. 4 Demonstration of caregiving-relevant scenarios using robotic e-skin with vertically integrated proximity and pressure sensor arrays. (a) Four representative phases of object detection: (i) approach toward the object, (ii) misaligned positioning, (iii) correct alignment, and (iv) contact with the object. Scale bars, 20 mm. (b) Calculated distance and pressure values corresponding to each phase in (a), based on the current signals measured from the optical and pressure sensor arrays, respectively. (c) Four representative phases of interaction with the human skin: (i) approach, (ii) soft contact, (iii) firm contact, and (iv) withdrawal. Scale bars, 30 mm. (d), (e) Calculated distance (d) and pressure (e) values corresponding to each phase in (c), based on the current signals measured from the optical and pressure sensor arrays, respectively.

signals of individual pixels under red and green illumination and compared with reference values obtained from a commercial pulse oximeter. The SpO_2 estimation followed a conventional approach, using the following ratio of ratios (R value):

$$R = \frac{AC_{Red}/DC_{Red}}{AC_{Green}/DC_{Green}}$$

The alternating current (AC) component reflects the periodic changes in blood volume due to cardiac pulsation, while the direct current (DC) component corresponds to the static absorption of tissues and non-pulsatile blood.[43,44] The rationale behind this calculation is that the ratio of AC to DC for each wavelength reflects the relative modulation of light absorption by pulsatile arterial blood. Since oxygenated and deoxygenated hemoglobin absorb red and green light differently, the R value serves as an indirect indicator of blood oxygen saturation.[45] As shown in Fig. 5(f), a linear calibration curve correlating SpO_2 and R values was established as:

$$SpO_2\ (\%) = 107 - 24R$$

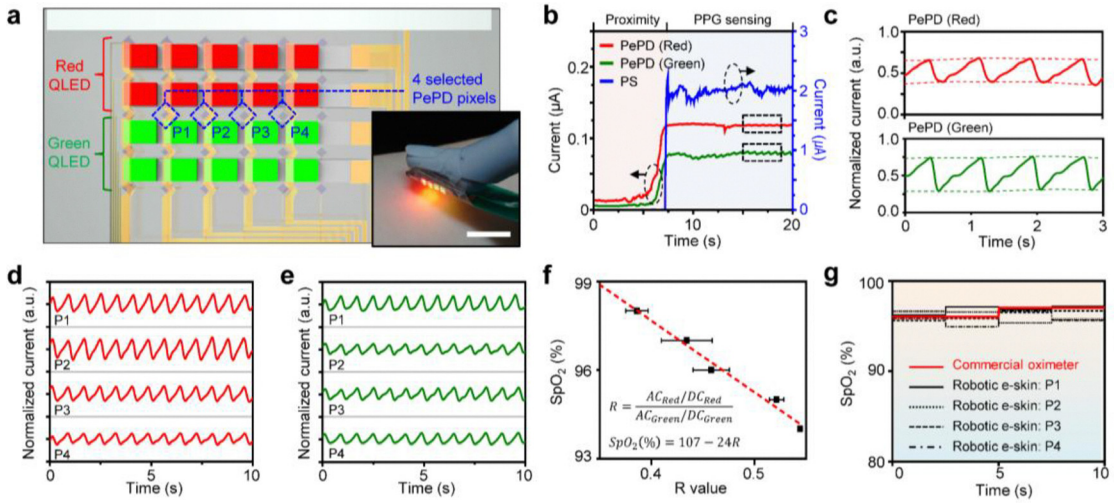

Fig. 5 PPG signal sensing and pulse oximetry using robotic e-skin. (a) Schematic illustration of the optical sensor array used for PPG signal sensing. The inset shows a photograph of the robotic fingertip integrated with the e-skin measuring biosignals. Scale bar, 30 mm. (b) Measured current responses from the optical sensor and pressure sensors before contact (proximity sensing mode) and after contact (PPG sensing mode). (c) Normalized current obtained under red (top) and green (bottom) QLED illumination, showing PPG waveforms. (d) and (e) Normalized current obtained from four different pixels under red (d) and green (e) QLED illumination. (f) Calibration curve showing the relationship between SpO_2 and the ratio of red to green signal amplitudes (R value). (g) Estimated SpO_2 values derived from the robotic e-skin (four individual pixels) compared with a commercial pulse oximeter.

Based on the calibration curve, SpO_2 data were estimated using 10-second segments of PPG signals. While most pixels produced SpO_2 estimates that closely matched the reference values obtained from a commercial pulse oximeter, minor deviations were observed across the array (Fig. 5(g)). These findings highlight the importance of considering spatial signal variability to ensure accurate biosignal interpretation. Moreover, with the future implementation of a higher-resolution array containing a greater number of pixels, it is expected that more detailed spatial analyses will be possible, enabling even more precise mapping of regional SpO_2 values.

3. Conclusions

In this study, we developed a multifunctional robotic e-skin featuring vertically integrated optical and tactile sensor arrays, designed for application in humanoid caregiving robots. The dual-mode optical sensor array, consisting of QLEDs and PePDs, enabled both proximity detection and PPG sensing, while the microstructured nanocomposite-based pressure sensor array provided sensitive and stable tactile feedback. System-level demonstrations in two representative caregiving-relevant scenarios validated the capabilities of the e-skin to inform key stages of human–robot interaction, including object localization, contact verification, and biosignal acquisition. The e-skin successfully captured PPG signals, and its pixelated architecture enabled spatially resolved sensing, enhancing measurement accuracy. Although the robotic finger used in this study was not part of an autonomous system and was not electrically integrated with the sensor outputs, we demonstrated that the e-skin signals can effectively provide information relevant to various stages of human–robot interaction.

Future efforts will focus on further enhancing the multifunctionality, electrical and optical performance, and mechanical/electrical stability of the e-skin platform to improve its scalability, ensure long-term operational reliability, and broaden its application scope. One key direction is the integration of the e-skin with robotic control systems to enable closed-loop, sensor-informed fingertip motions, which is an essential capability for autonomous caregiving robots.

Beyond proximity and PPG sensing, the integration of additional sensors for monitoring vital health parameters is critical for advancing robotic caregiving. In this context, the vertically stacked architecture offers significant advantages. It not only maximizes spatial efficiency and pixel density but also offers streamlined fabrication, making it suitable for incorporating additional sensing modalities such as temperature,[46–48] humidity,[49,50] and various electrophysiological signal sensors.[51–53]

The current prototype adopts an optimized configuration consisting of a 5 × 6 passive matrix of PePDs and a 4 × 5 array of QLEDs to enable dual-mode optical sensing. While this design effectively demonstrates the feasibility of multimodal sensing, achieving higher spatial resolution is essential for more precise mapping and cross-validation of signals. However, increasing the pixel density presents inherent trade-offs, including reduced pixel size and pitch, which can lead to decreased LED light output, lower proximity detection sensitivity, and increased optical and electrical crosstalk. Future advancements in the optoelectronic performance of flexible LEDs and PDs, combined with the integration of switching devices for active-matrix operation, could support higher-resolution sensing and enhance the scalability of the system architecture.

Ensuring long-term operational stability remains a significant challenge, as it involves preventing material leaching and

protecting internal components from environmental degradation. The current system utilizes a minimal organic encapsulation with a water vapor transmission rate (WVTR) of approximately 10^{-2} gper day m^{-2},[54] which provides limited barrier performance. To achieve extended reliability, more advanced encapsulation strategies are required. In particular, hybrid organic–inorganic encapsulation structures with ultra-low WVTRs below 10^{-6} g per day m^{-2} are promising candidates.[55,56] Addressing these encapsulation challenges will be critical to advancing our e-skin platform toward more durable, scalable, and context-aware applications in real-world environments.

In conclusion, this vertically integrated, multifunctional sensing platform represents a significant step toward enabling safe, precise, and context-aware human–robot interaction in next-generation caregiving technologies. Building on this foundation, further advancements in system integration, sensing diversity, and environmental durability can expand its impact across real-world assistive robotic systems.

4. Methods

4.1. Material preparation

Synthesis of colloidal QDs. Cadmium acetate ($Cd(OAc)_2$, 99.995%), cadmium oxide (CdO, >99.99%), zinc oxide (ZnO, 99.99%), zinc acetate ($Zn(OAc)_2$, 99.99%), sulfur (S, 99.99%), selenium (Se, 99.99%), oleic acid (OA, 90%), myristic acid (MA, >99%), 1-octadecene (ODE, 90%) and trioctylphosphine (TOP, 97%) were purchased from Sigma-Aldrich. Red- and green-emitting CdSe@ZnS quantum dots were synthesized following our previous work.[57] After purification, the quantum dots were dispersed in octane at a concentration of 25 mg mL^{-1} for solution processing.

Synthesis of ZnMgO nanoparticles. Zinc acetate dihydrate ($Zn(Ac)_2{\cdot}H_2O$, ≥99%), magnesium acetate tetrahydrate ($Mg(Ac)_2{\cdot}4H_2O$, ≥98%), tetramethylammonium hydroxide pentahydrate (TMAH, 98%) and dimethyl sulfoxide (DMSO) were purchased from Sigma-Aldrich. TMAH (5.5 mmol) was dissolved in 10 mL of ethanol to prepare the injection solution. Zinc acetate dihydrate (2.55 mmol) and magnesium acetate tetrahydrate (0.45 mmol) were dissolved in 30 mL of DMSO, into which TMAH solution was rapidly injected under stirring. The reaction was carried out for 1 hour at room temperature in a water bath. The product was purified by repeated centrifugation with ethyl acetate and ethanol, then redispersed in 10 mL of ethanol.

Material preparation for PePDs. Methylammonium bromide (MABr), formamidinium iodide (FAI) were purchased from Greatcell Solar Materials. Cesium iodide (CsI) and lead(II) Iodide (PbI_2) and lead(II) bromide ($PbBr_2$) were purchased from Alfa Aesar. To prepare the $(FA_{0.85}MA_{0.10}Cs_{0.05})Pb(I_{1.70}Br_{1.30})$ perovskite precursor, FAI (1.53 M), CsI (0.09 M), MABr (0.18 M), PbI_2 (0.72 M), and $PbBr_2$ (1.08 M) were dissolved in 1 mL of a DMF : DMSO mixed solvent (4 : 1 v/v) and stirred at 70 °C for 10 h until fully dissolved. The solution was then cooled to room temperature.

Preparation of the CNT–PDMS composite. Multi-walled carbon nanotube (MWCNT) dispersion (5 wt% in isopropyl alcohol) was purchased from Gratube, and PDMS(Sylgard 184) was purchased from Dow Corning Corporation. The MWCNT dispersion and PDMS (base : curing agent = 5 : 1 by weight) were mixed at a ratio corresponding to 7 wt% CNTs (PDMS : solid CNT = 93 : 7 by weight). The mixture was homogenized using a planetary centrifugal mixer (Thinky AR-100) for 1 minute. The total weight of the mixture was recorded, and the mixture was degassed at room temperature in a desiccator for 30 minutes. After degassing, the weight was re-measured to estimate the remaining solvent residue. Mixing (1 minute) and degassing (30 minutes) cycles were repeated to achieve the composite.

4.2. Device fabrication and integration

Fabrication of flexible QLED arrays. Glass substrates were cleaned with acetone and isopropyl alcohol, followed by O_2 RIE treatment (0.1 Torr, 30 W, 1 min). A Teflon layer (AF-2400) was coated on the glass substrate, then annealed to facilitate subsequent delamination. A bottom encapsulation layer was formed by depositing parylene-C (~1 μm) and SU-8 2000.5 (~0.3 μm). Bottom anodes consisting of Cr/Au (7/70 nm) and ITO (100 nm) were deposited using shadow masks. PEDOT:PSS was then spin-coated (2000 rpm, 50 s) and annealed at 150 °C for 30 min, after which the substrates were transferred into an argon-filled glovebox. TFB was spin-coated (2000 rpm, 30 s) and annealed at 150 °C for 30 min. For emissive layers, QD layers were either spin-coated (single-color emitting device) or transfer printed (multi-color emitting device) on HTL, followed by annealing at 150 °C for 30 min. The transfer printing process of the QD film was based on our previous work.[34] Subsequently, ZnMgO was spin-coated (2000 rpm, 30 s) and annealed at 120 °C for 30 min. A 50-nm-thick Al cathode was deposited through a shadow mask, and top encapsulation was deposited, consisting of parylene-C (~1 μm) and SU-8 2000.5 (~0.3 μm) bilayer.

Fabrication of flexible PePD arrays. A flexible passive matrix array of perovskite photodetectors (PePDs) was fabricated on a SiO_2 wafer. The wafer was cleaned using acetone and isopropyl alcohol, followed by O_2 RIE treatment (0.1 Torr, 30 W, 1 min). A 15 wt% polyimide (PI) solution was spin-coated at 8000 rpm for 60 s and sequentially annealed at 150 °C for 10 min, 180 °C for 30 min, and 250 °C for 2 h. Cr/Au (5/50 nm) was deposited by thermal evaporation and patterned into interconnection lines using photolithography. An epoxy insulating layer (SU-8 2000.5, ~0.3 μm) was spin-coated (2000 rpm, 30 s), patterned *via* photolithography, and annealed at 120 °C for 30 min to prevent electrical short-circuits. A second Cr/Au (10/100 nm) was then deposited and patterned into interdigitated electrodes using the same photolithographic procedure. The patterned substrates were transferred into an argon-filled glovebox, where the perovskite precursor solution was spin-coated at 4000 rpm for 40 s. Before the end of spinning, 0.5 mL of chlorobenzene was dispensed onto the rotating substrate to promote crystallization. The coated substrates were then annealed at 100 °C for 30 min. Finally, the substrates were removed from the glovebox

and immersed in 50 °C chloroform to pattern the perovskite films by lift-off.

Fabrication of flexible PS arrays. A flexible array of resistive pressure sensors was fabricated using a CNT–PDMS composite layer with molded microstructures. A Si wafer was first coated with a 20 μm-thick photoresist layer and patterned *via* grayscale photolithography to define the microstructured surface. After development, the wafer was vapor-treated with trichloro(1*H*,1*H*,2*H*,2*H*-perfluorooctyl)silane (FOTS) for 6 hours to facilitate PDMS demolding. 5 : 1 PDMS was cast onto the patterned wafer and cured at 70 °C for 2 hours to form a negative replica. After peeling off the cured PDMS mold from the photoresist master, its surface was again vapor-treated with FOTS to assist subsequent release of the CNT–PDMS composite film. A CNT–PDMS mixture was blade-coated onto the mold to fill the microstructures, cured at 70 °C for 2 hours, and peeled off to obtain a microstructured composite film. The sensor substrate was prepared following the same procedure used for the PePD array, involving sequential formation of a PI layer on a SiO_2 wafer and photolithographic patterning of interdigitated Cr/Au (10/100 nm) electrodes. A thermal release tape (TRT) was applied to selectively mask the interdigitated and contact pad regions, followed by spin-coating of diluted PDMS (PDMS : *t*-butanol = 1 : 1 w/w). After removing the TRT, the CNT–PDMS composite film was aligned such that its microstructured area covered the interdigitated electrode region, and the diluted PDMS layer was cured on a 100 °C hot plate for 30 minutes to complete the sensor fabrication.

Vertical assembly of flexible device components. To assemble the vertically integrated robotic e-skin, the PePD array was first delaminated using TRT and transferred onto a PET substrate spin-coated with d-PDMS (3000 rpm, 60 s) adhesive layer, followed by curing at 100 °C for 30 minutes. Separately, the fully encapsulated QLED array was spin-coated with d-PDMS, and the PePD array was flipped and laminated onto the QLED array using an optical alignment system (MDA-400 M, MIDAS system) with alignment keys, ensuring that the photodetector (PD) pixels were aligned without overlapping the underlying LED pixels. This stacked configuration formed a dual-mode optical sensing module. After thermal curing under the same conditions, d-PDMS was applied to the backside of the PET substrate. The pressure sensor substrate, comprising interdigitated Cr/Au electrodes on a PI layer, was then delaminated using TRT and laminated onto the optical module using the same alignment keys. The CNT–PDMS composite film was transferred using the same procedure as in the pressure sensor fabrication, followed by curing on a 100 °C hot plate for 30 minutes. Finally, the supporting glass substrate was carefully removed, and the encapsulation layer above the QLED contact pads was selectively etched by O_2 RIE (0.1 Torr, 150 W, 3 min 30 s). Flat flexible (FFC) jumper cables were bonded to the exposed contact pads to enable electrical interfacing. The fully assembled e-skin was trimmed to remove inactive regions and mounted onto a robotic fingertip using a membrane switch spacer for mechanical attachment.

4.3. Device characterization

The electrical and optical characteristics of QLEDs were evaluated using a source meter (Keithley 2636, Tektronix) and a spectroradiometer (CS-2000, Konica Minolta) to measure current density–voltage–luminance (*J*–*V*–*L*) characteristics and electroluminescence (EL) spectra. All current–voltage measurements for PDs and pressure sensors were performed using a semiconductor device parameter analyzer (B1500A, Agilent Technologies). The basic photoresponse of PDs was characterized under illumination from mounted commercial LEDs emitting at 530 nm and 625 nm (M530L4 and M625L4, Thorlabs). Proximity and other motion- or distance-dependent measurements were conducted using a custom-built displacement control system comprising a motorized stage and a precision screw-based actuator. Time-resolved responses of PDs and pressure sensors under modulated illumination were evaluated by applying square-wave optical inputs generated using a waveform generator (33511B, Agilent Technologies). For quantitative validation of PPG signal accuracy, a commercial pulse oximeter (CharmII, Charmcare) was used concurrently during measurements. Optical absorption spectra and photoluminescence spectra of QD solutions were measured using a UV-Vis-NIR spectrophotometer (Cary 5000, Agilent Technologies) and a fluorescence spectrometer (Fluoromax-4, Horiba), respectively. Transmission electron microscopy images of QDs were acquired using a Tecnai G2 F20 Twin TMP microscope (FEI). The morphology of the fabricated CNT–PDMS microstructures was examined using a scanning electron microscope (S-3400, Hitachi).

Ethical approval

This study was approved by the Institutional Review Board (IRB) of Seoul National University (IRB no. 2507/004-012).

Author contributions

H. Heo, J. Park, D.-H. Kim, and D. C. Kim conceived and designed the project. H. Heo, J. Park, H. Joo, and D. C. Kim developed the methodology. H. Heo, J. Park, and D. Ko performed the fabrication, measurement, and analysis of the sensor components and their integration into sensor arrays. K. Lee, J. Lee, and J. Yang synthesized and characterized the quantum dots. H. Heo, J. Park, G. D. Cha, D.-H. Kim, and D.C. Kim wrote and edited the manuscript. The project was jointly supervised and administered by D.-H. Kim, and D. C. Kim, who served as the corresponding authors.

Conflicts of interest

The authors declare that there are no conflicts of interest.

Data availability

All data generated or analyzed during this study are included in the article and SI. The data are available from the corresponding authors upon reasonable request.

Supplementary information is available: Characterization of QDs, transient photoresponse of PePDs, performance of optical proximity sensor under green QLED illumination, morphologies of the MWCNT/PDMS nanocomposite, and output current map of the optical and pressure sensor arrays. See DOI: **https://doi.org/10.1039/d5nh00418g**

Acknowledgements

This research was supported by the Institute for Basic Science under grant numbers IBS-R006-A1. This work was also supported by the DGIST R&D Program of the Ministry of Science and ICT (25-SENS2-04).

References

1 C. Xu, S. A. Solomon and W. Gao, *Nat. Mach. Intell.*, 2023, **5**, 1344–1355.
2 Y. Zhu, W. Moyle, M. Hong and K. Aw, *Sensors*, 2025, **25**, 2895.
3 W. Ji, R. Luo, Y. Sun, M. Yang, Y. Liu, H. Chen, D. Lin, Z. Su, G. Tao and D. Chen, *Research*, 2025, **8**, 0592.
4 S. Duan, Q. Shi, J. Hong, D. Zhu, Y. Lin, Y. Li, W. Lei, C. Lee and J. Wu, *ACS nano*, 2023, **17**, 1355–1371.
5 S. Padhan, A. Mohapatra, S. K. Ramasamy, S. Agrawal and S. Ramasamy, *Cureus*, 2023, 15.
6 T. J. Prescott and J. M. Robillard, *iScience*, 2021, **24**, 101993.
7 L. Zhang, S. Xing, H. Yin, H. Weisbecker, H. T. Tran, Z. Guo, T. Han, Y. Wang, Y. Liu and Y. Wu, *Nat. Commun.*, 2024, **15**, 4777.
8 J. Park, J. Mok, J. Ha, C. Choi and D. H. Kim, *FlexTech*, 2025, DOI: **10.1016/j.flextech.2024.100042**.
9 C. Choi, G. J. Lee, S. Chang, Y. M. Song and D. H. Kim, *Adv. Mater.*, 2024, **36**, 2412252.
10 M. Cai, Z. Jiao, S. Nie, C. Wang, J. Zou and J. Song, *Sci. Adv.*, 2021, **7**, eabl8313.
11 A. Miyamoto, S. Lee, N. F. Cooray, S. Lee, M. Mori, N. Matsuhisa, H. Jin, L. Yoda, T. Yokota and A. Itoh, *Nat. Nanotechnol.*, 2017, **12**, 907–913.
12 S. Lee, S. Franklin, F. A. Hassani, T. Yokota, M. O. G. Nayeem, Y. Wang, R. Leib, G. Cheng, D. W. Franklin and T. Someya, *Science*, 2020, **370**, 966–970.
13 S. Gong, W. Schwalb, Y. Wang, Y. Chen, Y. Tang, J. Si, B. Shirinzadeh and W. Cheng, *Nat. Commun.*, 2014, **5**, 3132.
14 H. U. Chung, A. Y. Rwei, A. Hourlier-Fargette, S. Xu, K. Lee, E. C. Dunne, Z. Xie, C. Liu, A. Carlini and D. H. Kim, *Nat. Med.*, 2020, **26**, 418–429.
15 J. H. Koo, Y. J. Lee, H. J. Kim, W. Matusik, D.-H. Kim and H. Jeong, *Annu. Rev. Biomed. Eng.*, 2024, **26**, 331–355.
16 X. L. Li, W. Z. Wang, B. Li, C. Chen, F. Q. Xu, Z. Y. Yang, X. S. Meng, Q. R. Yang, Q. Wang and Y. B. Zhu, *Adv. Mater.*, 2025, 2504266.
17 B. Wu, T. Jiang, Z. Yu, Q. Zhou, J. Jiao and M. L. Jin, *Adv. Sci.*, 2024, **11**, 2308560.
18 Z. He, H. Duan, J. Zeng, J. Zhou, X. Zhong, Z. Wu, S. Ni, Z. Jiang, G. Xie and J.-Y. Lee, *Sci. Adv.*, 2025, **11**, eads2834.
19 J. Byun, Y. Lee, J. Yoon, B. Lee, E. Oh, S. Chung, T. Lee, K.-J. Cho, J. Kim and Y. Hong, *Sci. Rob.*, 2018, **3**, eaas9020.
20 S. Chang, J. H. Koo, J. Yoo, M. S. Kim, M. K. Choi, D.-H. Kim and Y. M. Song, *Chem. Rev.*, 2024, **124**, 768–859.
21 R. Zhao, Z. Gu, P. Li, Y. Zhang and Y. Song, *Adv. Mater. Technol.*, 2022, **7**, 2101124.
22 T. Yokota, P. Zalar, M. Kaltenbrunner, H. Jinno, N. Matsuhisa, H. Kitanosako, Y. Tachibana, W. Yukita, M. Koizumi and T. Someya, *Sci. Adv.*, 2016, **2**, e1501856.
23 H. Jinno, T. Yokota, M. Koizumi, W. Yukita, M. Saito, I. Osaka, K. Fukuda and T. Someya, *Nat. Commun.*, 2021, **12**, 2234.
24 S. Li, J. H. Jang, W. Chung, H. Seung, S. I. Park, H. Ma, W. J. Pyo, C. Choi, D. S. Chung and D.-H. Kim, *ACS Nano*, 2023, **17**, 20013–20023.
25 G. D. Cha, D.-H. Kim and D. C. Kim, *Korean J. Chem. Eng.*, 2024, **41**, 1–24.
26 B. Du, S. Xiong, L. Sun, Y. Tagawa, D. Inoue, D. Hashizume, W. Wang, R. Guo, T. Yokota and S. Wang, *Sci. Adv.*, 2024, **10**, eadp2679.
27 H. S. Lee, B. Noh, S. U. Kong, Y. H. Hwang, H.-E. Cho, Y. Jeon and K. C. Choi, *npj Flexible Electron*, 2023, **7**, 15.
28 J. Park, H. Seung, D. C. Kim, M. S. Kim and D. H. Kim, *Adv. Funct. Mater.*, 2021, **31**, 2009281.
29 C. Son, J. Kim, D. Kang, S. Park, C. Ryu, D. Baek, G. Jeong, S. Jeong, S. Ahn and C. Lim, *Nat. Commun.*, 2024, **15**, 8003.
30 J. Kim, H. J. Shim, J. Yang, M. K. Choi, D. C. Kim, J. Kim, T. Hyeon and D. H. Kim, *Adv. Mater.*, 2017, **29**, 1700217.
31 T. Park, J. S. Kim, D. Ko, G. D. Cha, D.-H. Kim and D. C. Kim, *Korean J. Chem. Eng.*, 2024, **41**, 3517–3543.
32 M. K. Choi, J. Yang, T. Hyeon and D.-H. Kim, *npj Flexible Electron*, 2018, **2**, 10.
33 D. C. Kim, H. Yun, J. Kim, H. Seung, W. S. Yu, J. H. Koo, J. Yang, J. H. Kim, T. Hyeon and D.-H. Kim, *Nat. Electron.*, 2021, **4**, 671–680.
34 D. C. Kim, H. Seung, J. Yoo, J. Kim, H. H. Song, J. S. Kim, Y. Kim, K. Lee, C. Choi and D. Jung, *Nat. Electron.*, 2024, **7**, 365–374.
35 D. C. Kim, M. K. Choi, D.-H. Kim and J. Yang, *npj Flexible Electron*, 2025, **9**, 1–9.
36 L. Dou, Y. Yang, J. You, Z. Hong, W.-H. Chang, G. Li and Y. Yang, *Nat. Commun.*, 2014, **5**, 5404.
37 F. Wang, X. Zou, M. Xu, H. Wang, H. Wang, H. Guo, J. Guo, P. Wang, M. Peng and Z. Wang, *Adv. Sci.*, 2021, **8**, 2100569.
38 F. Liu, K. Liu, S. Rafique, Z. Xu, W. Niu, X. Li, Y. Wang, L. Deng, J. Wang and X. Yue, *Adv. Sci.*, 2023, **10**, 2205879.
39 T.-H. Kim, K.-S. Cho, E. K. Lee, S. J. Lee, J. Chae, J. W. Kim, D. H. Kim, J.-Y. Kwon, G. Amaratunga and S. Y. Lee, *Nat. Photonics*, 2011, **5**, 176–182.
40 J. Park, M. S. Kim, J. Kim, S. Chang, M. Lee, G. J. Lee, Y. M. Song and D.-H. Kim, *Sci. Rob.*, 2024, **9**, eadk6903.
41 P. M. Middleton, G. S. Chan, E. Steel, P. Malouf, C. Critoph, G. Flynn, E. O'Lone, B. G. Celler and N. H. Lovell, *Med. Biol. Eng. Comput.*, 2011, **49**, 859–866.
42 C. M. Lochner, Y. Khan, A. Pierre and A. C. Arias, *Nat. Commun.*, 2014, **5**, 5745.

43 J. Allen, *Physiol. Meas.*, 2007, **28**, R1.
44 K. H. Shelley, *Anesth. Analg.*, 2007, **105**, S31–S36.
45 T. Y. Abay and P. Kyriacou, *J. Clin. Monit. Comput.*, 2018, **32**, 447–455.
46 Q. He and Q. Zhang, *Optoelectron. Lett.*, 2021, **17**, 400–406.
47 J. Shin, B. Jeong, J. Kim, V. B. Nam, Y. Yoon, J. Jung, S. Hong, H. Lee, H. Eom and J. Yeo, *Adv. Mater.*, 2020, **32**, 1905527.
48 B. Zhang, W. Xu, L. Peng, Y. Li, W. Zhang and Z. Wang, *Nat. Rev. Electr. Eng.*, 2024, **1**, 218–233.
49 Y. Pang, J. Jian, T. Tu, Z. Yang, J. Ling, Y. Li, X. Wang, Y. Qiao, H. Tian and Y. Yang, *Biosens. Bioelectron.*, 2018, **116**, 123–129.
50 S. Li, Y. Zhang, X. Liang, H. Wang, H. Lu, M. Zhu, H. Wang, M. Zhang, X. Qiu and Y. Song, *Nat. Commun.*, 2022, **13**, 5416.
51 H. U. Chung, A. Y. Rwei, A. Hourlier-Fargette, S. Xu, K. Lee, E. C. Dunne, Z. Xie, C. Liu, A. Carlini and D. H. Kim, *Nat. Med.*, 2020, **26**, 418–429.
52 A. Miyamoto, S. Lee, N. F. Cooray, S. Lee, M. Mori, N. Matsuhisa, H. Jin, L. Yoda, T. Yokota and A. Itoh, *Nat. Nanotechnol.*, 2017, **12**, 907–913.
53 S. Kabiri Ameri, R. Ho, H. Jang, L. Tao, Y. Wang, L. Wang, D. M. Schnyer, D. Akinwande and N. Lu, *ACS nano*, 2017, **11**, 7634–7641.
54 M. K. Choi, J. Yang, D. C. Kim, Z. Dai, J. Kim, H. Seung, V. S. Kale, S. J. Sung, C. R. Park and N. Lu, *Adv. Mater.*, 2018, **30**, 1703279.
55 J. H. Kwon, E. G. Jeong, Y. Jeon, D.-G. Kim, S. Lee and K. C. Choi, *ACS Appl. Mater. Interfaces*, 2018, **11**, 3251–3261.
56 B.-H. Kwon, C. W. Joo, H. Cho, C.-M. Kang, J.-H. Yang, J.-W. Shin, G. H. Kim, S. Choi, S. Nam and K. Kim, *ACS Appl. Mater. Interfaces*, 2021, **13**, 55391–55402.
57 J. Yoo, K. Lee, U. J. Yang, H. H. Song, J. H. Jang, G. H. Lee, M. S. Bootharaju, J. H. Kim, K. Kim and S. I. Park, *Nat. Photonics*, 2024, **18**, 1105–1112.